Materials Science & Engineering A 893 (2024) 146109

Contents lists available at ScienceDirect

Materials Science & Engineering A

journal homepage: www.elsevier.com/locate/msea

Comparison of fatigue crack growth behaviour in electron-beam and laser powder-bed-fusion Inconel 718

Qiuyi Wang [a], Rui Bao [a,**], Binchao Liu [a], Songsong Lu [a], Hui Peng [b], Bo Chen [c,*]

[a] National Key Laboratory of Strength and Structural Integrity, Institute of Solid Mechanics, School of Aeronautic Science and Engineeing, Beihang University, Beijing, 100191, China
[b] Research Institute for Frontier Science, Beihang University, Beijing, 100191, China
[c] School of Engineering, University of Leicester, Leicester, LE1 7RH, UK

ARTICLE INFO

Keywords:
Fatigue crack growth
Microstructure
Digital image correlation
Additive manufacturing
Inconel 718

ABSTRACT

A comparative study on fatigue crack growth behaviour was made between the electron-beam powder-bed-fusion (PBF-EB) and laser powder-bed-fusion (PBF-LB) Inconel 718. The crack followed a transgranular path with a faster propagation rate for the PBF-EB Inconel 718, whereas a combination of intergranular and transgranular path was observed for the PBF-LB, and its slower rate being comparable to the wrought counterpart. The main fatigue crack in the PBF-EB Inconel 718 exhibited a sawtooth shaped path at the micro-scale, with intensive slip traces close to the crack surfaces owing to the very low work hardening rate. Based on the digital image correlation (DIC) analysis of the crack tip field, fatigue-crack sawtooth path in the PBF-EB Inconel 718 can be successfully predicted by using a strain energy density criterion, which dictates the crack growth follows the direction of minimum distance from the crack tip to elasto-plastic boundary. For the PBF-LB Inconel 718, the predominant fatigue crack was straight at low ΔK, but severe deflections occurred at the medium and high ΔK regimes. A clear correlation exists between the incipient intergranular cracks and the main crack path deflection. This suggests that once the accumulated damage in the plastic zone around the crack tip reaches the critical value, intergranular cracks can form the new front of the fatigue crack, causing the main crack path deflection. Elasto-plastic fracture mechanics parameters of r_p and ΔCTOD, derived from the DIC-based crack tip field analysis, can qualitatively predict the lower crack growth rate of the PBF-LB Inconel 718.

1. Introduction

It has been nearly a decade since powder-based additive manufacturing (AM) is established as a reliable means to process Inconel 718, a polycrystalline Ni-base superalloy with excellent materials performance at demanding environments and thus receiving a wide range of industrial applications, e.g., aerospace, oil and gas, and automotive [1,2]. The layer-wise nature, rapid solidification and micro-melt pool open many possibilities to tailor the crystallographic texture, grain morphology, and other microstructure features, enabling the location-specific properties of the AM Inconel 718 [3,4]. The vast majority of work focused on the microstructure evolution and mechanical properties under monotonic loading of AM Inconel 718 processed using various parameters such as heat source [5,6], build height [7], post-heat treatment [8–10], etc. Tensile properties [1,6,9] and the overall fatigue life [1,11,12] of AM Inconel 718 are comparable to that processed by conventional means.

Fatigue involves the initiation and growth of cracks due to cyclic loading with most of the failures under the stress level significantly lower than the yield point. Understanding and predicting the fatigue crack growth behaviour is a prerequisite for the development of damage tolerance assessment procedure which underpins the safe operation of engineering structures [13]. With increasing demands of using AM Inconel 718 to fabricate safety-critical parts/components, it becomes timely and important to improve our knowledge about the fatigue crack growth properties. The present work is specifically aimed at evaluating the fatigue crack growth behaviour at room temperature by comparison of electron beam powder bed fusion (PBF-EB) with laser powder bed fusion (PBF-LB) Inconel 718. The primary novelty of the work is to employ digital image correlation (DIC) technique to capture the crack

* Corresponding author.
** Corresponding author.
E-mail addresses: rbao@buaa.edu.cn (R. Bao), bo.chen@leicester.ac.uk (B. Chen).

https://doi.org/10.1016/j.msea.2024.146109
Received 31 July 2023; Received in revised form 27 December 2023; Accepted 7 January 2024
Available online 9 January 2024

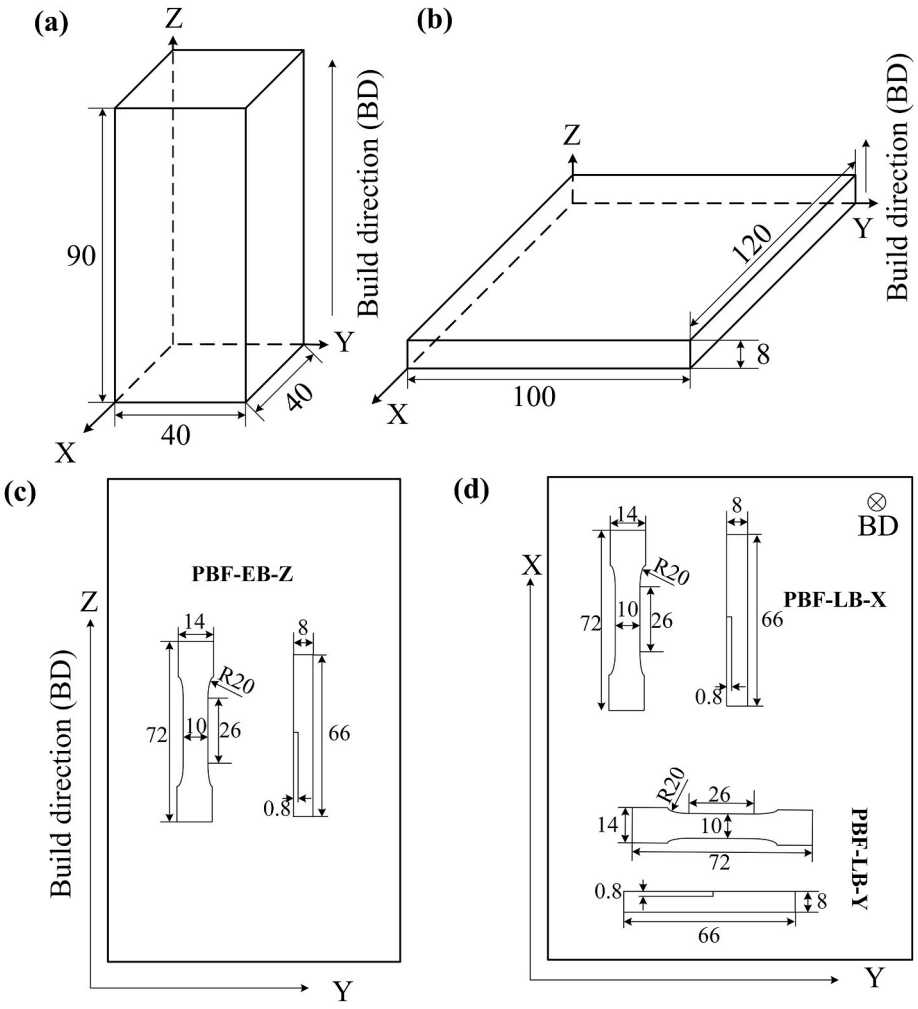

Fig. 1. a.m. Inconel 718 samples processed by PBF-EB in (a) and PBF-LB in (b); tensile and clamped single-edge-notch-tension (SENT) specimens extracted from the PBF-EB sample in (c) and PBF-LB sample in (d). All units are in mm.

tip field and then combine such information with microstructure observations to advance our knowledge about the controlling factor that alters the crack path and its propagation rate.

In terms of the stress intensity factor range (ΔK), Konecná et al. [14] found that PBF-LB Inconel 718 in the as-built condition had a nearly identical resistance to the fatigue crack growth in the high ΔK region of >15 MPa • $\sqrt{m}$, when compared to the wrought counterpart. However, the stress intensity factor range threshold (ΔK_{th}) of the PBF-LB Inconel 718 was significantly lower than the wrought material. This was attributed to the lower B content of 32 ppm, higher residual stress and finer grain size of ~10 μm. Gruber et al. [15] observed that the PBF-LB Inconel 718 in the as-built condition had a similar fatigue crack growth rate and fracture mode when compared to that in the hot-isostatic-pressed condition, despite a significantly reduced ductility. Brynk et al. [16] found that Re addition can effectively lower the crack growth rate in the PBF-LB Inconel 718.

Role of microstructures on the fatigue crack growth behaviour was studied in detail by Yu et al. in Ref. [17] on directed energy deposition (DED) Inconel 718, and by Ramanathan et al. in Ref. [18] on both the PBF-EB and PBF-LB Inconel 718. It was found that the coarse Laves phase with uneven γ''/γ' precipitates can severely increase the crack growth rate [17]. Also, the soft precipitate-free zone adjacent to the short-acicular δ-phase was partly responsible for the faster crack growth rate as the ease of dislocation slips at this region. To some extent, the above-mentioned observation was not in line with the work by Ramanathan et al. [18], where the fatigue crack growth behaviour was found to be unaffected by the precipitates such as NbC, TiN and δ-phase. They further concluded that grain size had a strong influence on the fatigue crack growth mode by studying the size range from 20 to 80 μm. However, their conclusion was based on high-cycle fatigue tests instead of fatigue crack growth tests.

The build orientation dependence of fatigue crack growth behaviour in AM Inconel 718 was attributed to the grain shape and texture. Brynk et al. [16] observed that the 45° oriented specimen of PBF-LB Inconel 718 had the lowest crack growth rate among the three orientations of 0°, 45° and 90°. Ghorbanpour et al. [19] studied the PBF-LB Inconel 718 with functionally graded microstructure, and an increased crack growth rate was found together with the crack deflection when the pre-cracked specimen was loaded perpendicular to the build direction, whereas little difference for that when loaded parallel to the build direction. Balachandramurthi et al. [20] studied PBF-EB Inconel 718, revealing that the growth mode was transgranular when the crack grew perpendicular to the build direction; whereas a combination of intergranular and transgranular modes for the loading parallel to the build direction. Deng et al. [21] investigated the dwell-fatigue crack behaviour of PBF-EB Inconel 718, and they found that the specimen loaded parallel to the build direction showed a better dwell-fatigue cracking resistance when compared to that of perpendicular to it.

To summarise, literature does exist regarding the role of microstructures on fatigue crack growth behaviour in AM Inconel 718 processed by the PBF-LB and PBF-EB methods as majority whilst DED as minority. These studies revealed that columnar grain shape, texture and

Table 1
Chemical compositions of PBF-EB and PBF-LB Inconel 718 as measured using inductively coupled plasma atomic emission spectroscopy (ICP-AES) (all in wt.%).

	Ni	Cr	Fe	Nb	Mo	Co	Ti	Al	Mn	Si	C
PBF-EB	51.63	18.71	20.13	5.05	3.09	0.011	1.05	0.57	<0.01	0.019	0.064
PBF-LB	51.67	18.56	19.69	5.10	3.00	0.032	0.96	0.62	0.034	0.1	0.046

precipitates can all impact on the fatigue crack growth behaviour. Nevertheless, the interaction between the fatigue crack tip field and local microstructure features is yet to be explored. Our hypothesis is that an improved understanding of the coupling effect will help to unravel the underlying mechanisms for the crack growth behaviour. It is also important to note that the DIC-based crack tip field technique is not limited to the AM Inconel 718. Instead, this method can apply to other material systems, such as AM Ti–6Al–4V [22,23].

2. Material and experimental

2.1. PBF-EB and PBF-LB samples

The PBF-EB sample was processed on an Arcam A2xx machine with a voltage of 60 kV and under a controlled vacuum of 0.01 mbar with high purity helium used as regulating gas. Standard cross-snake type scanning strategy was used during the hatch melt, together with the scan rotation of 90° between layers and layer thickness of 70 μm. Average beam current of 20 mA, scan speed of 6500 mm/s and focus offset of 17 mA were utilised. The printing parameter set was the optimised one based on our previous work on Ni-base superalloys [24,25]. A fully densified PBF-EB sample build was fabricated with dimensions of 40 × 40 × 90 mm^3, Fig. 1(a). All the in-process observation suggested good process stability (e.g., no smoke phenomenon or bumpy top surface).

The PBF-LB sample was processed on a Farsoon 301 M machine using the alternating X/Y raster scanning strategy and with the scan rotation of 67° between layers. A layer thickness of 30 μm was used in the PBF-LB process. Scan speed of 1000 mm/s and laser power of 240 W were utilised to produce the sample with dimensions of 100 × 120 × 8 mm^3, Fig. 1(b). More details about the PBF-LB sample fabrication can be found elsewhere [26].

Both the PBF-EB and PBF-LB samples were subjected to the solution treatment and precipitate ageing, which included firstly, heat treating at 980 °C for 1 h; secondly, ageing at 720 °C for 8 h, followed by furnace cooling to 620 °C at rate of 50 °C/h, and final ageing at 620 °C for 8 h. This chosen heat treatment procedure is expected to promote the precipitation of well-defined γ′ and γ″ while maintaining the grain shape and structure characteristic of the AM method, according to the previous work [9,17]. Chemical compositions as measured on the post-heat treated samples are given in Table 1. It is evident that these two types of AM Inconel 718 are virtually the same in terms of their bulk chemical compositions.

2.2. Tensile tests

Tensile specimens were extracted from the sample builds in such a way that the loading direction was parallel to the Z-build direction for the PBF-EB (Fig. 1(c)), whereas perpendicular to the Z-build for the PBF-LB (Fig. 1(d)). For the latter, both the X and Y orientations were tested to examine the in-plane orientation dependence. Throughout this paper, specimen ID has been defined to indicate the loading direction with respect to the coordinate system of the AM build. For example, PBF-LB-X means the tensile loading was along X direction. Tensile tests were performed using INSTRON 8801 servo-hydraulic fatigue test system under constant crosshead rate of 0.26 mm/min in accordance with ASTM E8/EBM-21. Three individual tests were conducted per sample condition, and extensometer with gauge length of 12.5 mm was attached to measure the strain.

2.3. Fatigue crack growth tests

Fatigue crack growth tests were conducted using clamped single-edge-notch-tension (SENT) specimens under stress ratio of $R = 0.1$ (P_{min}/P_{max}) and frequency of 0.9 Hz at ambient temperature. The specimen dimensions are given in Fig. 1(c) and (d). The tests were performed in accordance with ASTM E647-15. For the PBF-EB sample, SENT specimen was loaded along the Z-build direction, and hence abbreviated as PBF-EB-Z. By comparison, SENT specimens were loaded along X and Y, respectively, alike to the tensile specimens made of PBF-LB sample. This means that for specimen PBF-LB-X, the load was along

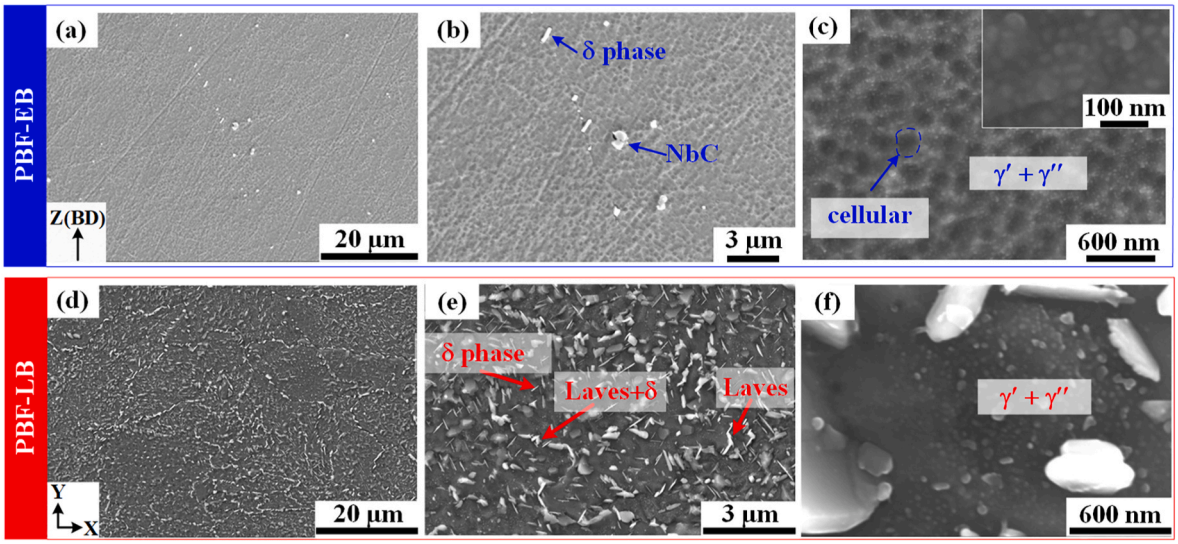

Fig. 2. SEM images: (a), (b) and (c) PBF-EB on XZ plane showing the characteristics of both the matrix and precipitates; (d), (e) and (f) PBF-LB on XY plane showing the features of both the matrix and precipitates.

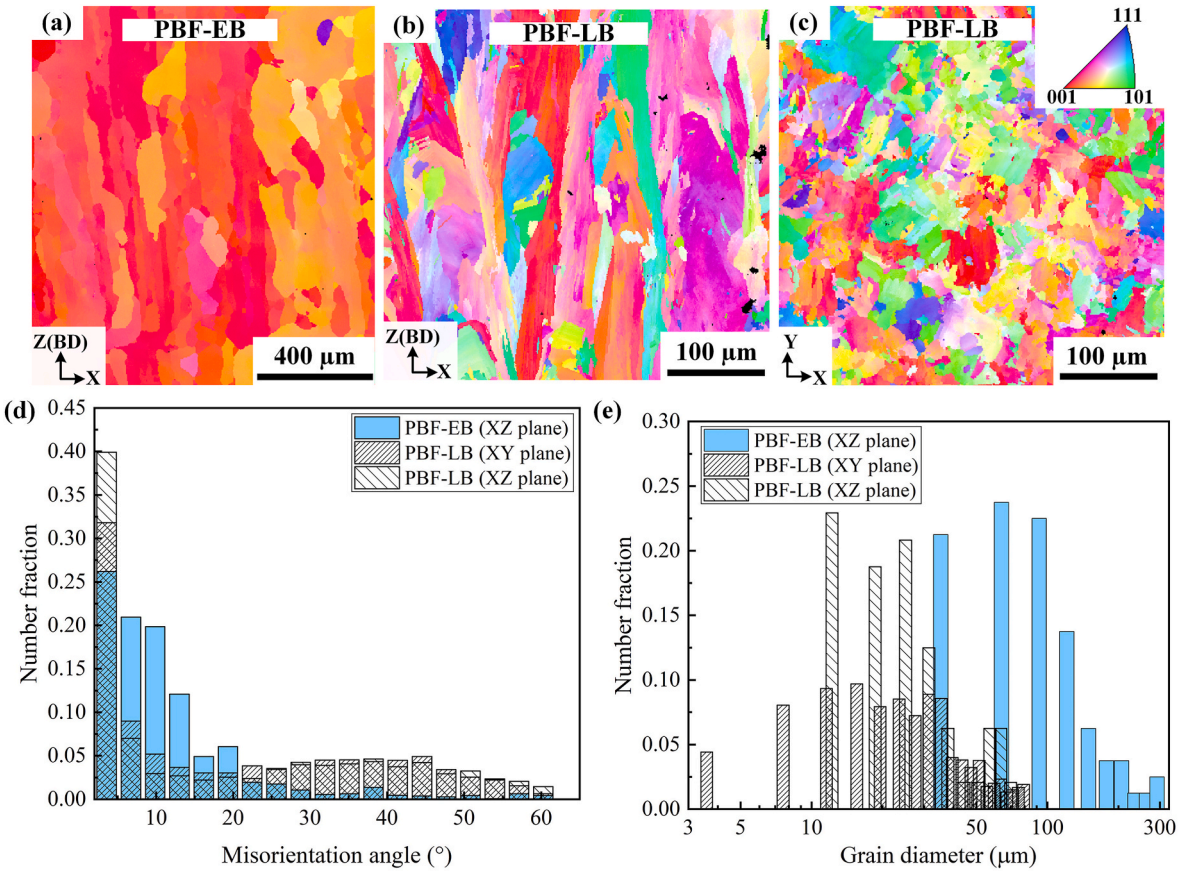

Fig. 3. (a) EBSD inverse pole figure (IPF-Z) maps of PBF-EB specimen in the XZ plane, in comparison with (b) PBF-LB specimen in the XZ plane and (c) XY plane; (d) GB orientation distribution histograms; (e) grain size distribution histograms. The IPF map legend is consistent throughout this paper.

X-direction, and the crack propagation was supposed to follow Y-direction. Maximum load (P_{max}) of the PBF-EB-Z specimen was 156 MPa and that of the PBF-LB-X and PBF-LB-Y specimens was 190 MPa.

Two opposite surfaces of each SENT specimen were mechanically polished with 1200-grit sandpaper to generate random scratches, which served as speckles for the digital image correlation (DIC) technique. All the fatigue crack growth experiments were conducted using a 5 kN IBTC-5000 in-situ fatigue tester (CARE Measurement & Control Test System Co., Ltd), equipped with ZEISS Axioscope optical microscope with 50x objective lense. The field-of-view provided by the charge coupled device (CCD) camera was 2.49 × 1.99 mm (resolution of 0.90 μm/pixel) with the crack path located at the centre of the image. Images were taken from the crack tip and the region nearby for every 15 – 20 MPa stress change and this procedure covered the entire fatigue loading and unloading cycle to enable the DIC-based determination of the crack tip field. Image taken under the zero load was used as the reference to calculate the displacement field.

2.4. Microstructure characterisations

To help elucidating the role of microstructures on fatigue crack growth behaviour, metallographic samples were prepared by mechanical grinding and polishing, followed by chemical etching in a solution of 100 ml HCl +100 ml C_2H_5OH + 5 g $CuCl_2$. A Zeiss G300 scanning electron microscopy (SEM), equipped with energy dispersive spectroscopy (EDS) detector was used for general microstructure observation. A JSM-7900F SEM equipped with the electron backscatter diffraction (EBSD) detector was employed to analyse the crystallography. EBSD data acquisition was carried out using step sizes of 1 μm and 3 μm, and Channel 5 software was used for data processing.

3. Results

3.1. Microstructures of the PBF-EB and PBF-LB Inconel 718

Representative SEM micrographs taken from the PBF-EB Inconel 718 are shown in the top row of Fig. 2. The low-magnification SEM micrograph of Fig. 2(a) shows that precipitates can be linearly distributed within the matrix. According to the SEM-based EDS analysis, these precipitates were confirmed as the needle shaped δ phase with enrichment of Nb, and blocky NbC phase with its size of up to 2 μm, Fig. 2(b). This observation agrees with the previous PBF-EB Inconel 718 work [27], reporting the needle shaped δ phase of ~200 nm and blocky MC carbides of ~1.5 μm. The figure inset in Fig. 2(c), which represents a high-magnification SEM micrograph, shows that the spherical γ″/γ′ precipitates of 40 nm are uniformly distributed in the matrix. The shape and size of the precipitates are consistent with the previous work [17]. Moreover, the matrix is characterised by the cellular sub-structures with the cell size of 200 nm, Fig. 2(b) for the overview and (c) for the detailed view.

Compared to the PBF-EB, PBF-LB Inconel 718 has a significantly higher volume fraction of precipitates, Fig. 2(d). These precipitates have two types in general: needle shaped δ phase and chain-like Laves phase, Fig. 2(e). These two phases are often adjacent to each other, due to the dissolution of Nb-rich Laves phase at the interdendritic region followed by re-precipitation as the δ phase [16]. The high-magnification SEM micrograph of Fig. 2(f) shows the presence of γ″/γ′ precipitate-free zone in the vicinity of the Laves and δ phases. The microstructural features in the present PBF-LB Inconel 718 are consistent with the literature [28–30], where the Laves and δ phases were found to be two primary precipitates in addition to the γ″/γ′ precipitates.

To examine the crystallographic texture and grain boundary type,

Table 2
Tensile properties of PBF-EB and PBF-LB processed Inconel 718.

Process	Elastic modulus E (GPa)	Yield strength $\sigma_{0.2}$(MPa)	Tensile strength σ_b(MPa)	Elongation (%)
PBF-EB-Z	108.1 ± 3.2	1105.5 ± 0.4	1154.7 ± 3.1	>16[a]
PBF-LB-X	197.0 ± 5.6	1092.3 ± 7.5	1358.5 ± 7.9	10.9 ± 2.5
PBF-LB-Y	135.3 ± 4.8	986.9 ± 4.1	1254.2 ± 26.3	11.6 ± 2.9
PBF-EB [9]	106.8	1087.8	1175.2	21.7
PBF-EB [37]	115.3	925.0	1138.0	15.7
PBF-LB [10]	166.8	711.0	1110.0	24.5

[a] Tensile test was continued without the extensometer attached as the sample elongation exceeded the extensometer maximum range.

EBSD analyses were performed on both the PBF-EB and PBF-LB specimens. For the PBF-EB Inconel 718, columnar grains are aligned with their long axis almost parallel to Z-direction and <001> is the preferred orientation, Fig. 3(a). The inverse-pole-figure (IPF) map in Fig. 3(a) include 144 grains, from which the average grain width was measured as 98 μm, Fig. 3(e), and nearly 80 % of grain boundaries (GBs) have the type of low-angle boundaries (LAGBs) defined by using the misorientation angle of <15°, Fig. 3(d). The observed predominant <001> texture for the PBF-EB Inconel 718, with the multiple uniform distributions (MUD) value of 26.8, is consistent with the previous work [9]. But the presence of high number density of LAGBs in the XZ plane of PBF-EB Inconel 718 was rarely reported, especially when compared to the PBF-LB material revealing only 50 % of LAGBs in both the XY and XZ planes, Fig. 3(d). The grain size of the PBF-LB Inconel 718 is considerably smaller than the PBF-EB sample, Fig. 3(e) with the average size determined as 40 μm and 30 μm for the XZ and XY planes of the PBF-LB sample, respectively. The IPF map of the XZ plane of the PBF-LB Inconel 718 is shown in Fig. 3(b), revealing those seemingly near-equiaxed grains under the XY plane are actually columnar grains. The MUD value for the {001} orientation of PBF-LB Inconel 718 was found as 4.53 for the XY plane while 6.31 for the XZ plane, suggesting a considerably lower texture when compared to the PBF-EB sample. Overall, the EBSD revealed microstructure characteristics are the same as those reported previously [6,31,32].

3.2. Tensile properties

Three individual tensile tests were performed per sample condition, with the average value of tensile properties summarised in Table 2 and representative tensile engineering stress-strain curves illustrated in Fig. 4(a). Overall, the PBF-EB Inconel 718 has a significantly lower elastic modulus (E) and ultimate tensile strength (σ_b), but higher yield strength ($\sigma_{0.2}$) and tensile ductility, in comparison with the PBF-LB Inconel 718. The strength difference is probably due to the finer grain structure in the PBF-LB Inconel 718 [33]. The lower E value of 108.1 ± 3.2 GPa in the PBF-EB-Z specimen can be attributed to its preferred <001> orientation, given that the directionally solidified <001> single-crystal Ni-base superalloy is only 60 % of the isotropic polycrystalline superalloys. In the work by Deng et al. [9] on both the as-built and heat-treated PBF-EB Inconel 718, the E value was measured to be 100–110 GPa under the tensile loading parallel to the build direction. It was also commented in Refs. [34,35] that the strong <001> texture along the build direction led to the low E value. Moreover, the PBF-EB Inconel 718 exhibits an ideal elasto-plastic characteristic, namely, an extremely low strain hardening rate over the plastic deformation, Fig. 4(b). Such an ideal elasto-plastic behaviour of PBF-EB Inconel 718 was also reported previously [36]. By comparison, the PBF-LB Inconel 718 has a much higher strain hardening rate, as manifested in the work hardening rate vs. true strain curve of Fig. 4(b).

Given a near-equiaxed grain structure observed in the XY plane, Fig. 3(c), one would expect an isotropic tensile behaviour, i.e., the similar tensile curve of PBF-LB-X and PBF-LB-Y. However, Fig. 4(a) shows anisotropic tensile properties with respect to the loading directions. The values of E, $\sigma_{0.2}$ and σ_b obtained from the tensile tests with the loading direction parallel to X direction (PBF-LB-X) are consistently higher than those with loading direction parallel to Y direction (PBF-LB-Y). No significant ductility was found between the two directions. The like-for-like comparison of the present tensile properties with the literature cannot be performed as only the tensile curve with the loading direction parallel to Z-build direction was available (e.g., Ref. [10]).

Before presenting the fatigue crack growth behaviour of the PBF-EB and PBF-LB Inconel 718, it is useful to summarise the similarities and key differences with respect to their microstructure and static tensile properties. First, the PBF-EB Inconel 718 has a significantly larger grain size than the PBF-LB counterpart. Second, the higher fraction of LAGBs but lower fraction of precipitates was found in the PBF-EB sample. Third, the strain hardening rate of the PBF-LB Inconel 718 was much higher than the PBF-EB counterpart exhibiting an ideal elasto-plastic

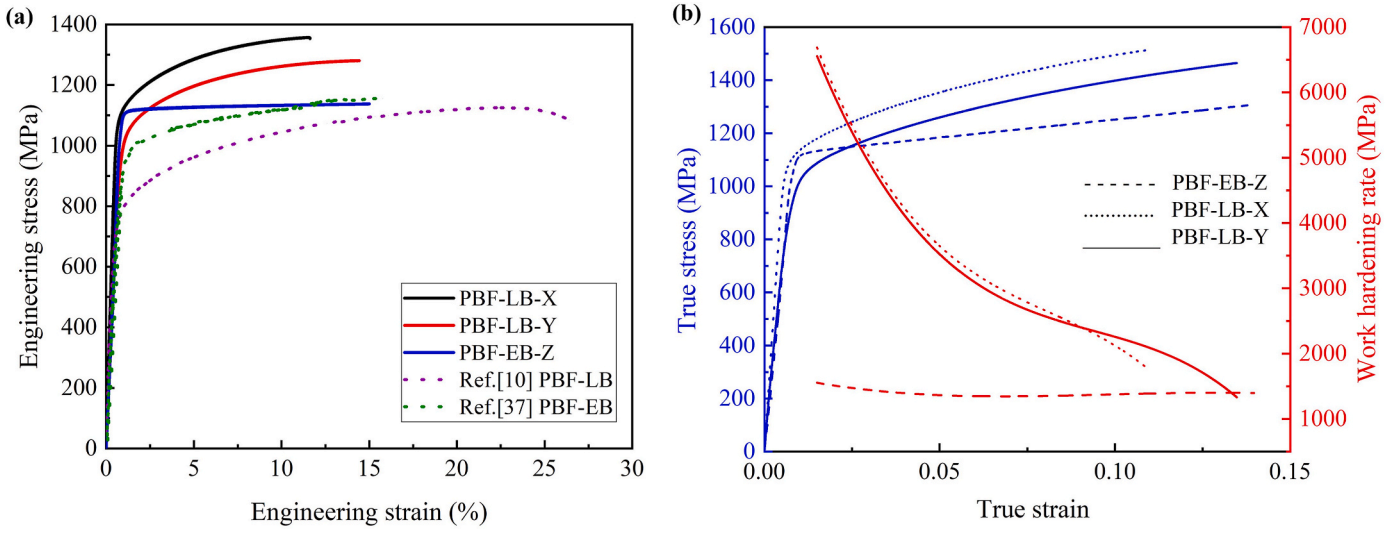

Fig. 4. Tensile properties of PBF-LB and PBF-EB Inconel 718: (a) engineering stress-strain curves and (b) true stress-strain curves together with the derived work hardening rate curves.

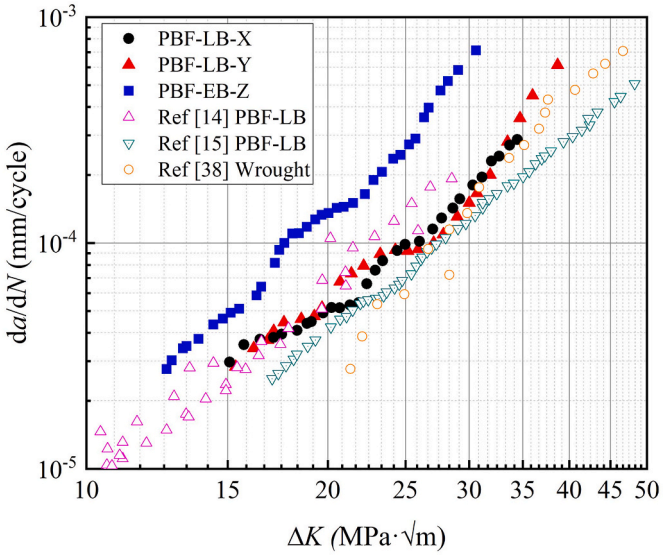

Fig. 5. Comparison of fatigue crack growth rates of the present AM Inconel 718 with the previous work on both the AM and wrought Inconel 718.

behaviour. Let's also reiterate that the fatigue crack growth behaviour which will be presented next involve three specimens: 1) PBF-EB-Z with the fatigue loading axis parallel to Z-build and crack is expected to propagate along Y; 2) PBF-LB-X with the fatigue loading axis parallel to X-direction and crack is expected to propagate along Y; and 3) PBF-LB-Y with the fatigue axis parallel to Y-direction and crack is expected to propagate along X. These chosen fatigue loading directions are the same as those used for tensile tests.

3.3. Fatigue crack growth behaviour

Typical fatigue crack growth rate plot of da/dN vs. ΔK in the value range of 14–40 MPa • $\sqrt{m}$ for the PBF-EB and PBF-LB Inconel 718 is shown in Fig. 5, revealing a second stage fatigue crack growth behaviour (i.e., a stable crack growth following the Paris law) for all three specimens. The fatigue crack growth rate of the PBF-EB-Z is faster than that of the PBF-LB-X and PBF-LB-Y, Fig. 5. Despite the anisotropic tensile properties between the PBF-LB-X and PBF-LB-Y, Table 2, the two orientations have a similar fatigue crack growth rate. The material constants of the Paris law were determined as $C = 3.98 \times 10^{-9}$ and $n = 3.48$ for PBF-EB-Z, 8.88×10^{-9} and 2.79 for PBF-LB-X, and 1.25×10^{-8} and 2.92 for PBF-LB-Y, respectively. Fig. 5 also compares the present data with the literature data, and it can be seen that the crack growth rate of the PBF-LB Inconel 718 is comparable to the previous PBF-LB work [14, 15] as well as the wrought material [38]. Unfortunately, the second-stage fatigue crack growth rate of the PBF-EB Inconel 718 could not be found in the literature to allow a data comparison.

The crack path of the PBF-EB Inconel 718 is shown in Fig. 6, revealing an overall straight propagation path at the macro-scale, Fig. 6 (a), while a sawtooth shaped path at the micro-scale with the presence of slip traces at both sides of the crack path, Fig. 6(b) and (c). The entire development of slip traces from beginning to the end can be clearly observed during the crack propagation (refer to Appendix A for more details). With the increasing ΔK value, the region showing the slip traces becomes wider and more pronounced, as highlighted by the dashed lines which outline the region boundaries in Fig. 6(a). It is evident in Fig. 6(b) that both sides of the fatigue crack show clear slip lines oriented about 45° direction towards left or right with respect to the vertical loading axis. It seems that the actual fatigue crack has chosen either of these two directions to grow and then re-selected the crack growth direction after a certain crack-length extension. With the further increase of crack length, i.e., $\Delta K = 29.1$ MPa • $\sqrt{m}$ in Fig. 6(c), the fatigue crack no longer

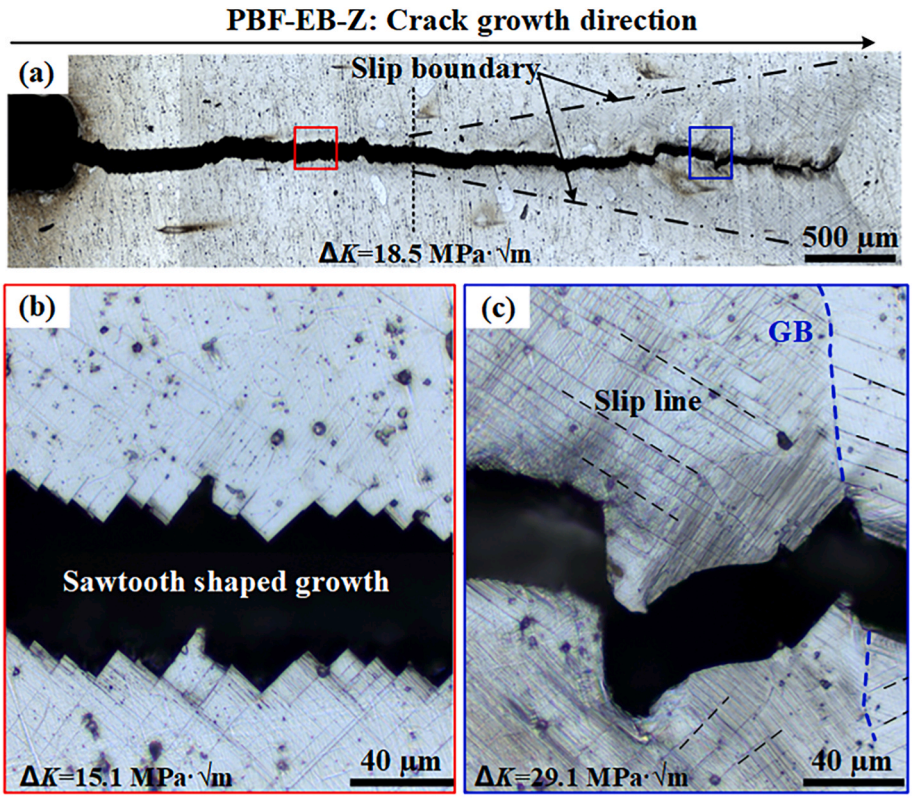

Fig. 6. Fatigue crack growth path of PBF-EB specimen: (a) crack path overview; (b) and (c) enlarged views of the indicated regions in (a) with the former taken from the region of $\Delta K = 15.1$ MPa • $\sqrt{m}$ and the latter from $\Delta K = 29.1$ MPa • $\sqrt{m}$.

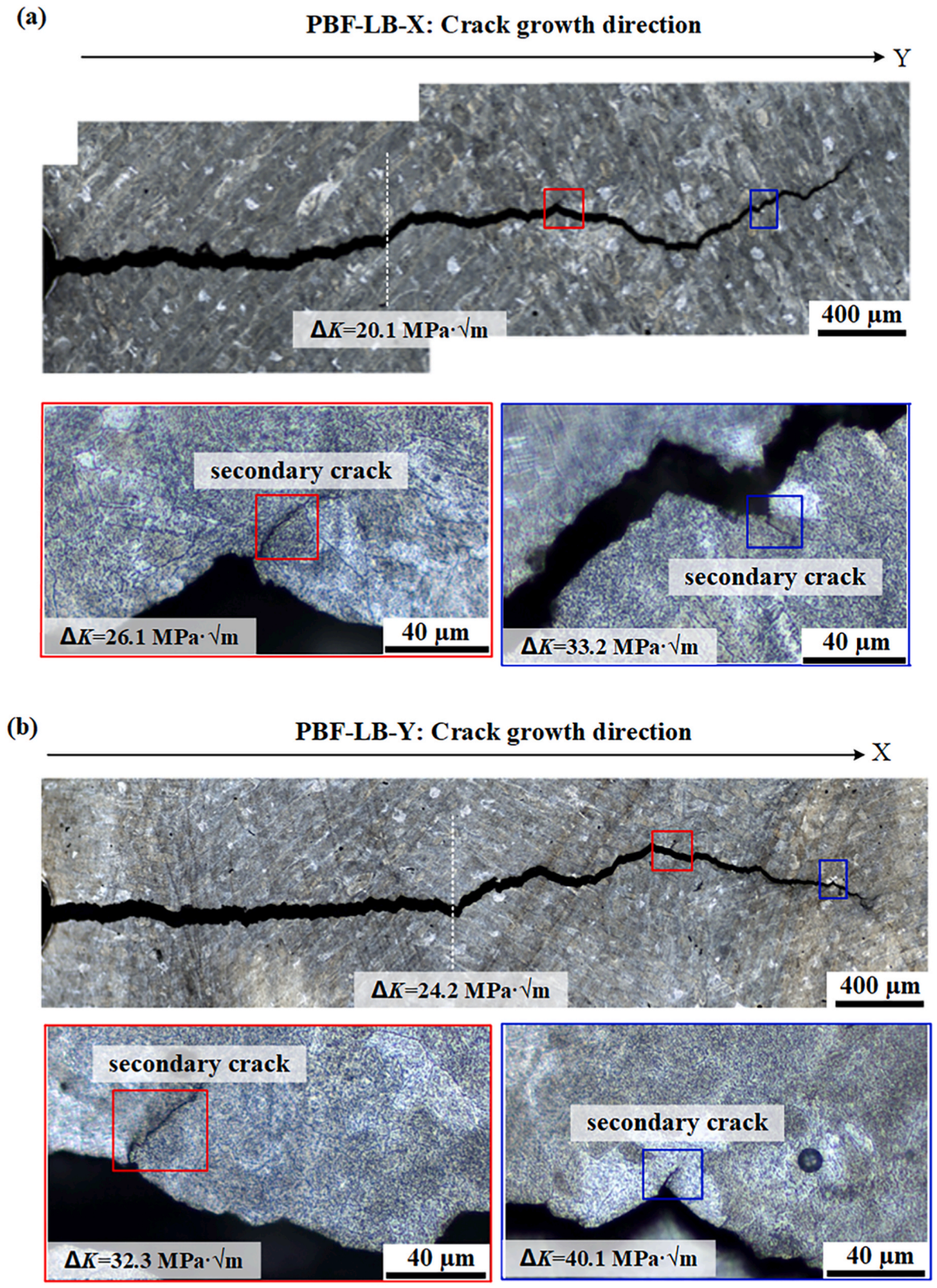

Fig. 7. Comparison of the fatigue crack growth path of the PBF-LB-X specimen in (a) with the PBF-LB-Y specimen in (b). The upper figure shows the crack path overview, while the enlarged views are given in the lower two figures.

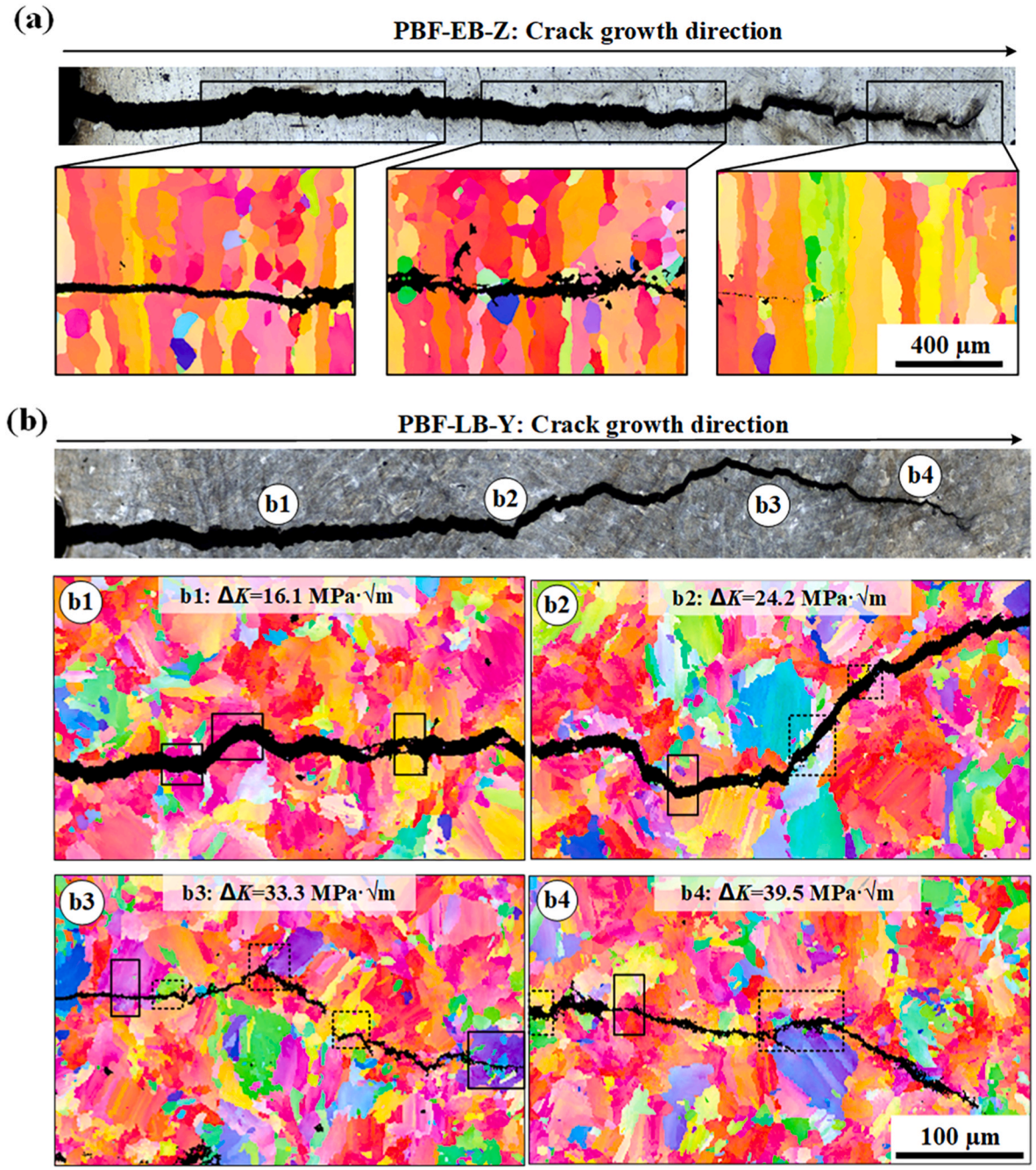

Fig. 8. EBSD orientation maps taken adjacent to the fatigue crack growth path: (a) PBF-EB-Z specimen; (b) PBF-LB-Y specimen. Black solid rectangles highlight regions with transgranular feature, whilst black dotted rectangles highlight those with intergranular mode. Number indicated regions correspond to ΔK value of 16.1, 24.2, 33.3 and 39.5, from position b1 to b4, respectively.

grows following the slip lines and the crack path edges become smoother. At this region the crack starts approaching the final unstable fracture.

For the PBF-LB Inconel 718, the overall crack growth direction is perpendicular to the loading direction under the low ΔK regime, but the macroscopic crack deflection occurs at the middle and high ΔK regimes. The incipient crack deflection from the pure Mode-I path occurs at $\Delta K >$ 20.1 MPa $\bullet \sqrt{m}$ for the PBF-LB-X specimen, Fig. 7(a), and $\Delta K >$ 24.2 MPa $\bullet \sqrt{m}$ for the PBF-LB-Y specimen, Fig. 7(b), respectively. The deflection direction can be upward or downward. The enlarged views as shown in Fig. 7 indicate that short secondary cracks often appear at the location where the main crack exhibits a deflection. Unlike the fatigue crack path of the PBF-EB-Z specimen (Fig. 6), the PBF-LB specimens do not have the sawtooth shaped propagation feature. Instead, the crack surfaces are relatively smooth, and without the slip line at either side surfaces along the path, see enlarged views in Fig. 7. Given little difference was found between the PBF-LB-X and PBF-LB-Y specimens, only the PBF-LB-Y specimen was subjected to the post-mortem EBSD examination.

Fig. 8 presents a series of EBSD orientation maps taken from different ΔK values along the fatigue crack growth path. The PBF-EB specimen shows a typical transgranular feature, and the vertical columnar grain boundaries do not seem to cause any deflection at the macro-scale, Fig. 8 (a). By comparison, the PBF-LB-Y specimen shows a combination of intergranular and transgranular crack growth mechanisms, as highlighted using the black dotted and solid rectangles in Fig. 8(b),

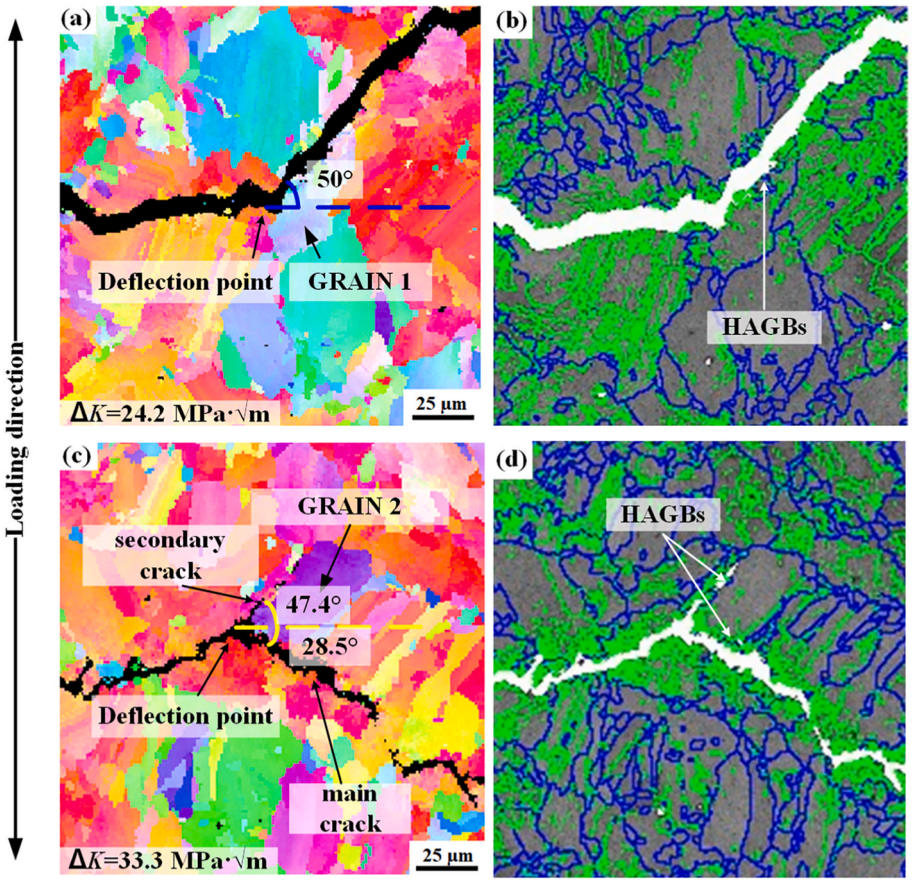

Fig. 9. EBSD orientation maps and GB angle diagrams around the fatigue crack growth path of PBF-LB-Y specimen: (a)&(b) fatigue crack deflecting; (c)&(d) fatigue crack branching. Green lines represent low angle grain boundaries (<15°),blue lines represent high angle grain boundaries (>15°). (For interpretation of the references to colour in this figure legend, the reader is referred to the Web version of this article.)

respectively. Especially, the mixed crack propagation mode appears towards the middle and high ΔK regimes, and the intergranular propagation seems to play a certain role on the crack path deflection.

4. Discussion

4.1. Effect of microstructure on fatigue crack growth path

It is recognised that the crack growth path is controlled by both the local microstructure and the crack-tip field. For the PBF-LB Inconel 718, with the increase of ΔK, the crack growth mechanism is switched from the transgranular to a combination of intergranular and transgranular modes, Figs. 7 and 8(b). Fig. 9(a) and (b) are a pair of EBSD maps with the former showing the grain orientation and the latter showing the grain boundary characters. The main fatigue crack is deflected upward by 50° when it reaches the location of GRAIN 1, followed by the trigger of intergranular cracking. The fraction of LAGBs adjacent to the crack surfaces seems to be consistently higher than the region away from the main crack. The sources of LAGBs near the crack path may not be solely attributed to the fatigue-induced phenomenon. This is because previous work has frequently reported the presence of high LAGBs in the as-built condition of Inconel 718 [39]. As also revealed in the present work, the PBF-LB Inconel 718 in the as-built condition has a considerably high fraction of LAGBs, Fig. 3(d). These LAGBs generally appear within the grains. Severe plastic deformation may be appeared around the crack tip when the main crack propagates steadily under the fatigue loading. Localised plastic deformation around the crack tip can cause high-density dislocation stacking, and their re-arrangement leads to the formation of LAGBs, which have also been commented in Refs. [40,41]. Moreover, at the deflection point where the crack propagates along the grain boundary of GRAIN 1, low number density of LAGBs can be seen in Fig. 9(b). This suggests that the time was not long enough to accumulate the local plasticity around the crack tip. It was reported in Ref. [42] that the misorientation between the two grains can affect the intergranular fatigue crack propagation path.

In the condition of high ΔK, tendency to form intergranular fatigue crack becomes higher, which is evidenced by the presence of short secondary cracks at the triple junction of grain boundaries, Fig. 9(c) and (d). When entering the triple junction, the main fatigue crack had two potential paths to choose: one was 47.4° upward and the other was 28.5° downward as indicated in Fig. 9(c). With the cyclic loading, the main crack eventually selected the easy direction to continue its propagation, whereas the incremental crack growth in the other direction became a non-propagating short secondary crack, so called crack branching. The reason for the main crack following the downward direction is probably due to its lower angle with respect to horizontal direction, i.e., more inclined for a Mode-I cracking. The above analysis assumes a similar cohesive strength between the upper and lower boundaries. It is worthwhile to emphasise that the secondary fatigue cracks with intergranular manner in the PBF-LB Inconel 718 only appeared when the main fatigue crack developed to a certain length, i.e., when ΔK reaches a threshold value. This implies that the magnitude of crack-tip field affects the crack deflection via cracking the grain boundary. For metals with large grains, macroscopic crack branching or even splitting due to secondary cracks at grain boundaries under fatigue, has been frequently observed when the stress intensity factor reaches a certain threshold, which has been recognised as a necessity for triggering crack initiation [43,44].

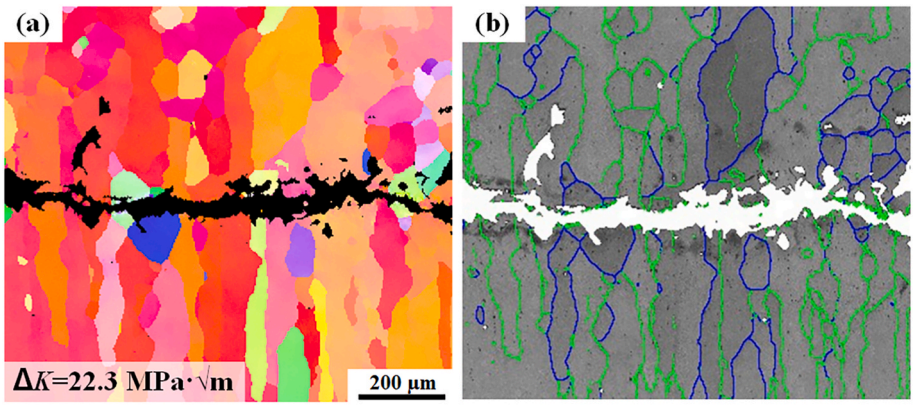

Fig. 10. Fatigue crack growth path of the PBF-EB-Z specimen: (a) EBSD orientation map, and (b) band contrast map overlaid with HAGBs (blue) and LAGBs (green). (For interpretation of the references to colour in this figure legend, the reader is referred to the Web version of this article.)

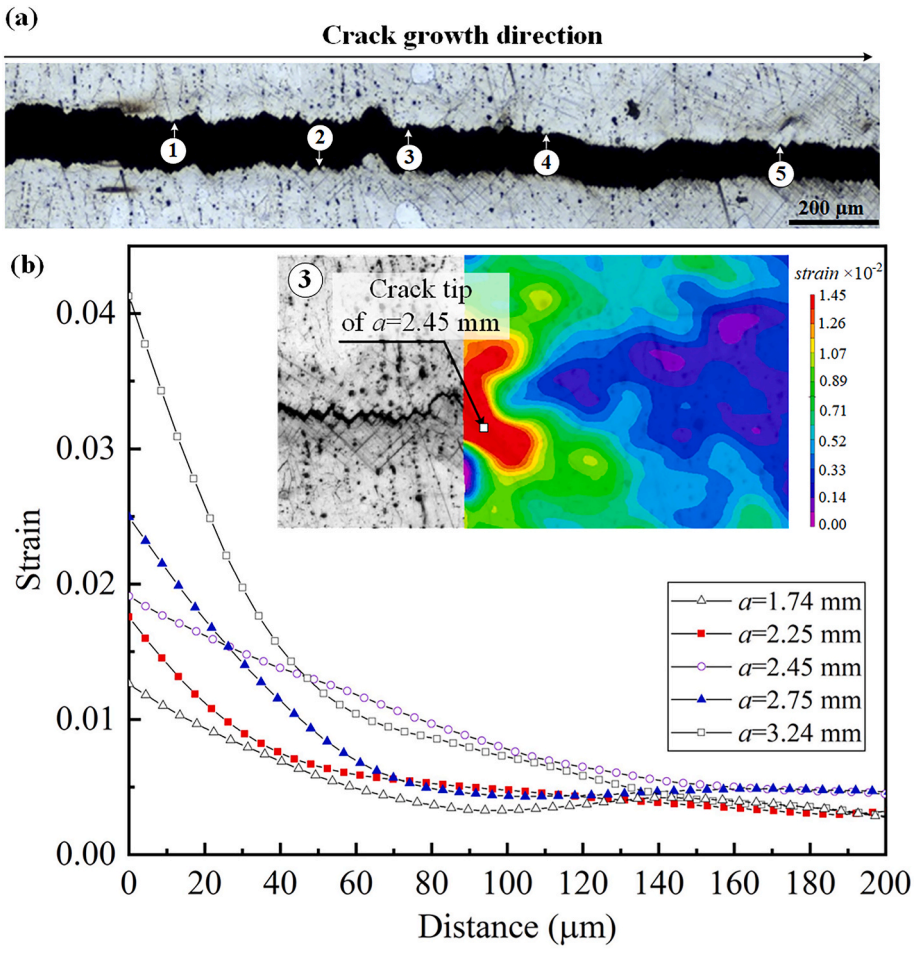

Fig. 11. (a) Five typical positions on the crack path; (b) typical crack tip strain field at position 3 and strain along the path front of crack tip at five typical positions of PBF-EB-Z specimen.

To summarise, for the PBF-LB Inconel 718 with small grain size of 30 μm in average, the plastic zone at the crack tip is small for a short crack length, and thereby the crack quickly grows out of the plastic zone, causing elastic unloading of the regions behind the crack. As a result, the accumulated damage is not sufficient to crack the adjacent grain boundaries. However, with the crack length increases, the plastic zone at the crack tip becomes larger and the time for crack to pass through the plastic zone is longer. Thus, the accumulated damage in the plastic zone around the crack tip is increased. When the damage accumulates to the critical value, intergranular cracks can form the new front of the fatigue crack, causing the main crack path deflection.

For the PBF-EB Inconel 718, fatigue crack was confirmed as transgranular all the way through the steady-state crack growth, Fig. 8(a), and the crack growth rate was considerably higher than the PBF-LB counterpart, Fig. 5. Fig. 10 presents a pair of EBSD maps taken from the ΔK value of 22.3. From the band contrast map in Fig. 10(b), it is evident that the fraction of LAGBs close to the crack surfaces is not higher than the region away from the main crack. Nearly all LAGBs as

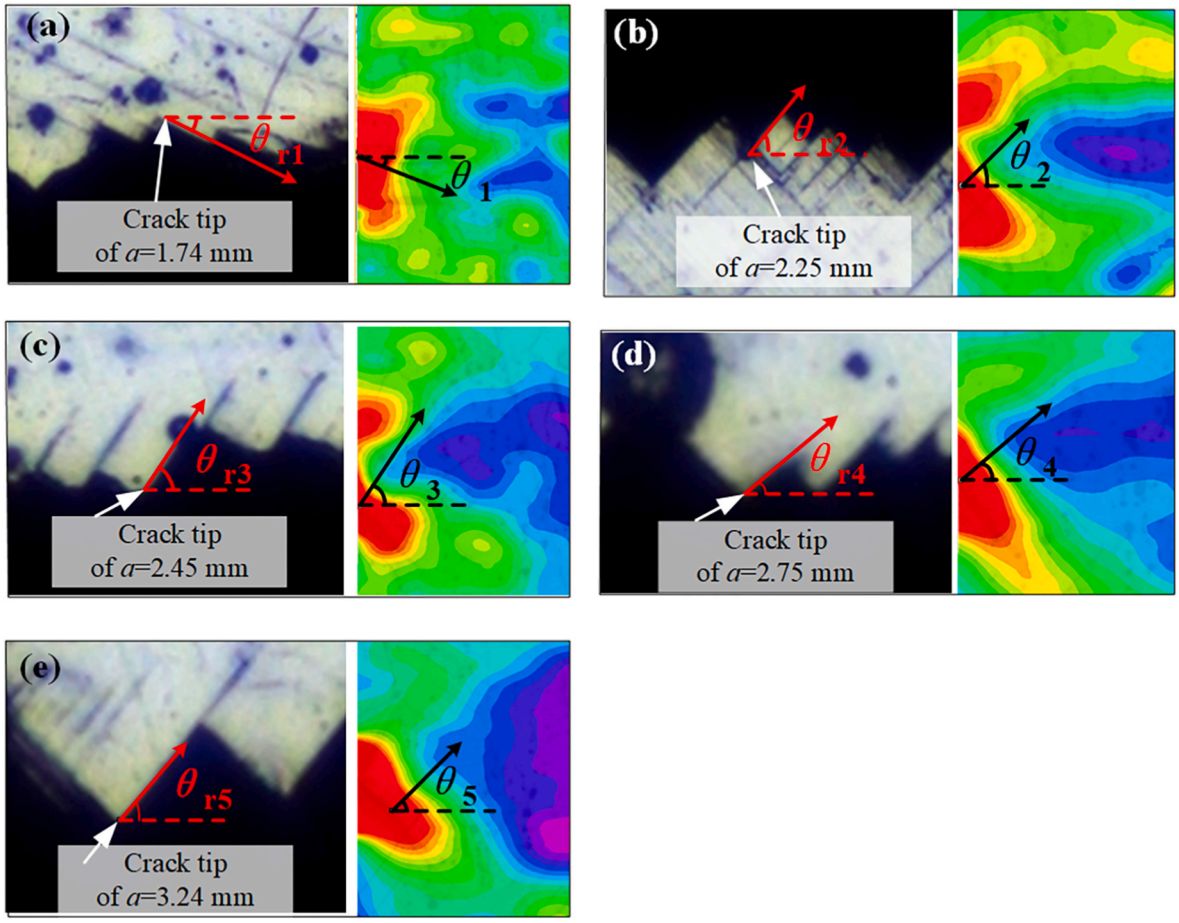

Fig. 12. Plots of actual deflection angles and predicted deflection angles by using strain energy density criterion at different crack-length positions: (a) $a = 1.74$ mm; (b) $a = 2.25$ mm; (c) $a = 2.45$ mm; (d) $a = 2.75$ mm; (e) $a = 3.24$ mm.

observed in the post-fatigued specimen are already existed in the prior-to-fatigue condition, Fig. 3(d). This finding can be attributed to the fact that the main crack grew out of the plastic zone too quickly to induce any dislocation stacking. Furthermore, the vertical HAGBs by nature are not favourable for initiating a secondary crack under the Mode-I fatigue loading. In the low-cycle fatigue work by Balachandramurthi et al. [20] on PBF-EB Inconel 718, it also revealed a transgranular crack, with its propagation direction perpendicular to the build direction. To summarise, local microstructure seems to play a minor role in determining the fatigue crack growth behaviour in the PBF-EB Inconel 718.

4.2. DIC based analysis of the crack tip field

Despite the fatigue crack path of the PBF-EB Inconel 718 is straight at the macro-scale, Fig. 6(a), the enlarged view reveals a clear and consistent sawtooth shape at the micro-scale, Fig. 6(b). In other words, the fatigue crack propagates in a zigzag manner, i.e., with the alternating 90° direction change. Here an attempt is made to establish the relationship between the DIC measured crack-tip field and crack growth direction. Five typical locations along the crack path are indicated in Fig. 11(a), with the crack length determined as 1.74 mm, 2.25 mm, 2.45 mm, 2.75 mm and 3.24 mm, respectively. DIC-based crack-tip field analysis was performed for each location, with an example illustrated in the figure inset of Fig. 11(b) for the crack length of $a = 2.45$ mm. The crack-tip field is not entirely symmetric with respect to the horizontal axis, probably owing to the sawtooth shape of the crack path. The main plot of Fig. 11(b) compares strain variations along a 200 μm horizontal line drawn from the front of the crack tip, i.e., perpendicular to fatigue loading direction. It can be seen that the crack tip strain decreases rapidly with the increasing distance and then reaches a plateau at distance of about 140 μm away from the crack tip. With the crack length increases, the strain at the crack tip becomes greater and the distance required for the strain to reach the plateau becomes longer.

Table 3
Comparison of predicted and actual crack deflection angles at different crack lengths.

Position (mm)	Actual angle θ_r (°)	Predicted angle by θ (°)	
		Strain energy density	Maximum circumferential strain
1: 1.74	24.5	21.8	41.6
2: 2.25	46.3	44.5	61.8
3: 2.45	58.1	57.5	59.1
4: 2.75	42.3	41.7	53.4
5: 3.24	48.5	44.7	43.1

To predict the direction of a mixed-mode crack growth, there are two groups of criteria in the literature: one is the energy-based criteria such as strain energy density criterion [45], and the other is stress or strain-based criteria such as the maximum circumferential strain criterion [46,47]. For the strain energy density criterion, the crack is assumed to grow along the direction of minimum distance from crack tip to elasto-plastic boundary. For simplicity, the elasto-plastic boundary is defined when the DIC-determined crack tip strain field exceeding the 1 % total strain. Fig. 12 compares the experimentally observed crack direction change with respect to the horizontal direction with the predicted value based on strain energy criterion at five different locations, i.e., crack length of 1.74 mm, 2.25 mm, 2.45 mm, 2.75 mm and 3.24 mm,

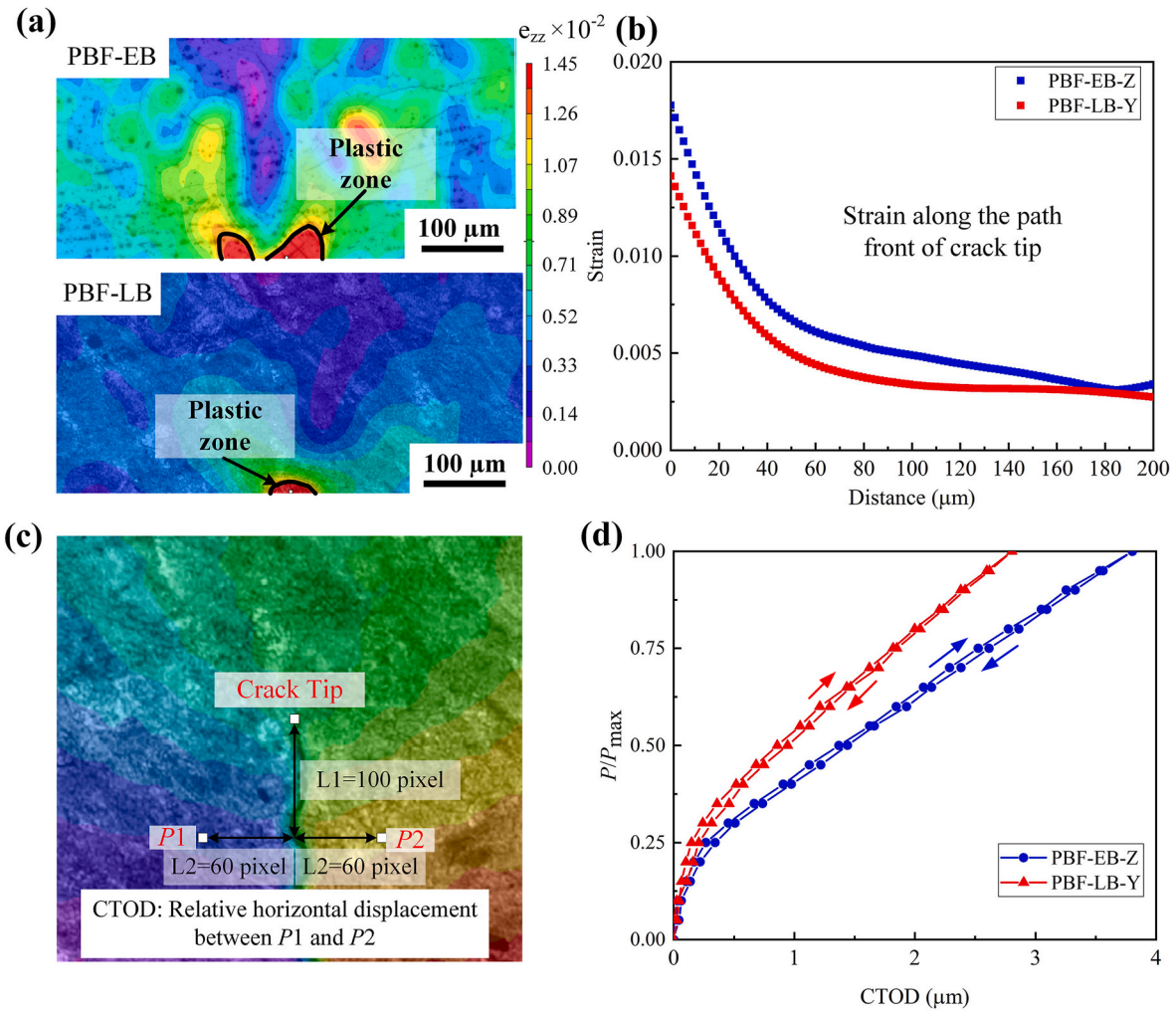

Fig. 13. (a) Comparison of the crack tip strain field between the PBF-EB and PBF-LB specimens; (b) strain along the path front of crack tip; (c) crack tip displacement field and schematic diagram of CTOD measurement; (d) plots of CTOD through a complete loading cycle of the PBF-EB and PBF-LB specimens.

respectively. The experimental observation agrees reasonably well with the model prediction in terms of the angle change, as summarised in Table 3. By comparison, the crack growth prediction based on the maximum circumferential strain criterion shows poor performance. Thus, the strain energy density criterion based on the crack tip field can predict the crack growth direction of the PBF-EB specimen at the micro-scale.

However, the applicability of the above-mentioned method to predict the fatigue crack growth direction for PBF-LB specimens was found to be not good. This is because the crack deflections are mainly caused by the change of fatigue crack growth mode when encountering the grain boundary (Fig. 9). Although the crack tip field may provide the evaluation of the driving force for the fatigue crack growth, it cannot consider the intrinsic resistance of crack growth which is related to the grain boundary in the present case. For PBF-LB specimens with small grains and many grain boundaries in the crack tip area, many factors could affect the actual direction of crack growth. Therefore, it is difficult to predict the direction of fatigue crack growth based on the crack tip field alone.

When the fatigue crack growth rate (da/dN) is plotted against ΔK, the PBF-EB specimen consistently shows a faster rate than the PBF-LB counterpart, Fig. 5. For such a plot, the influencing factors related to the microstructure are all considered using the fitting parameters of C and n as adopted in the Paris law. This classical approach is based on the linear elastic fracture mechanics. However, the DIC-based crack tip field analysis provides an alternative route to characterise the fatigue crack growth behaviour more precisely. For example, some elasto-plastic fracture mechanics parameters such as cyclic plastic zone size r_p [48] and crack tip opening displacement (CTOD) [49] can be extracted from the DIC images. An attempt was thus made to assess their capabilities to characterise the driving force for fatigue crack growth, with the aim to reconcile the different crack growth rate between the PBF-EB and PBF-LB Inconel 718. Similarly, the cyclic plastic zone boundary is defined when the DIC-determined crack tip strain field exceeding the 1 % total strain. DIC images of the crack-tip field for both sample builds under the similar ΔK value are shown in Fig. 13(a), together with the line plot showing the strain variation, revealing that the range of plastic zone at the crack tip for the PBF-EB specimen is significantly larger. This is because the PBF-EB Inconel 718 exhibits an ideal elasto-plastic behaviour as shown in Fig. 4, with an extremely low work hardening rate. More specifically, the PBF-EB specimen which has a ΔK value of 16.31 MPa • $\sqrt{m}$, slightly lower than that of 17.63 MPa • $\sqrt{m}$ for the PBF-LB specimen, shows a 33 % faster crack growth rate.

The plastic zone size (r_p) is defined as the minimum distance from the crack tip to elastoplastic boundary, and the r_p value was determined as 22.38 μm and 13.43 μm for the PBF-EB and PBF-LB specimens, respectively, Fig. 13(a). Moreover, the CTOD value defined by using the relative displacement between the fixed points on both sides of the crack surface, in which two points with horizontal distance of L1 = 100 pixel (89.55 μm) after the crack tip and vertical distance of L2 = 60 pixel

Table 4
Fracture mechanics parameters as derived from the DIC measurements on both the PBF-EB and PBF-LB specimens.

	da/dN (mm/cycle)	ΔK ($MPa\bullet\sqrt{m}$)	r_p (μm)	ΔCTOD (μm)
PBF-EB	5.86×10^{-5}	16.31	22.38	3.80
PBF-LB	4.46×10^{-5}	17.63	13.43	2.81
Ratio of the PBF-EB over PBF-LB data	1.33	0.92	1.66	1.35

(55.73 μm) away from the crack path were taken as measurement points, as shown in Fig. 13(c). The CTOD curves during one typical cycle are shown in Fig. 13(d), in which the crack closure can be identified when $P/P_{max} < 0.25$. However, after the crack is fully opened, the CTOD value of the PBF-EB specimen is greater than that of PBF-LB specimen under the same load, which accords with the observations of plastic zone size and crack-tip strains in Fig. 13(a) and (b). As a result, the range of CTOD in this loading cycle, ΔCTOD, turns out to be 3.80 μm and 2.81 μm for the PBF-EB and PBF-LB specimens, respectively.

Table 4 summarises three types of fracture mechanics parameters, i.e. stress intensity factor range ΔK, cyclic plastic zone size r_p, and crack-tip opening distance range ΔCTOD, for two different AM built Inconel 718. The PBF-EB specimen which shows a 33 % faster crack growth rate, has 8 % lower ΔK, 66 % higher r_p and 35 % higher ΔCTOD than the PBF-LB specimen. This suggests that the elasto-plastic fracture mechanics parameters can better reconcile the different crack growth rate between the PBF-EB and PBF-LB Inconel 718. The better performance of using the ΔCTOD over r_p may lie in the fact that ΔCTOD takes into account the variations during the whole loading cycle (especially crack closure effects), while the r_p approach does not.

5. Conclusions

Fatigue crack growth behaviour of the PBF-EB and PBF-LB Inconel 718 has been studied, with particular focus to the role of microstructure and crack-tip field. The following conclusions can be drawn.

(1) The PBF-EB sample has considerably lower elastic modulus and extremely low work hardening rate when compared to the PBF-LB counterpart, but the former has a higher yield strength and ductility despite a lower ultimate tensile strength. Most of these differences can be attributed to the considerably large columnar grains, strong <001> texture and high fraction of LAGBs in the PBF-EB sample.
(2) Fatigue crack growth rate of the PBF-EB specimen is faster than that of PBF-LB counterpart. The PBF-EB specimen shows a transgranular crack mechanism at the macro-scale, with the crack perpendicular to the fatigue load over the entire range of ΔK studied, but it presents a sawtooth-shaped path at the micro-scale.
(3) By comparison, the PBF-LB specimen shows the transgranular crack growth mode at low ΔK, but it changes to a combined transgranular and intergranular mechanism as the ΔK increases. The intergranular mode is manifested by the presence of secondary cracks which usually triggers the crack path deflection at the macro-scale.
(4) Using the strain energy density criterion combined with the DIC determined crack-tip filed, the sawtooth-shaped path characterised by the alternating 90° direction change of the crack at the micro-scale can be predicted.
(5) The higher fatigue crack growth rate in the PBF-EB Inconel 718 can be qualitatively explained by using DIC determined elasto-plastic fracture mechanics parameters, such as the crack tip opening displacement range (ΔCTOD) ranked the best and cyclic plastic zone size (r_p) as the second.

CRediT authorship contribution statement

Qiuyi Wang: Investigation, Methodology, Validation, Writing – original draft, Writing – review & editing. **Rui Bao:** Conceptualization, Methodology, Resources, Supervision. **Binchao Liu:** Investigation, Validation. **Songsong Lu:** Funding acquisition, Methodology. **Hui Peng:** Methodology, Resources. **Bo Chen:** Conceptualization, Funding acquisition, Investigation, Project administration, Supervision.

Declaration of competing interest

The authors declare that they have no known competing financial interests or personal relationships that could have appeared to influence the work reported in this paper.

Data availability

Data will be made available on request.

Acknowledgements

The authors gratefully acknowledge the financial support from The Postdoctoral General Foundation (2021M700338) and Bo Chen acknowledges financial support from the UK's Engineering and Physical Sciences Research Council, EPSRC First Grant Scheme (EP/P025978/1) and Early Career Fellowship Scheme (EP/R043973/1).

Appendix A. Observation of slip lines during the crack propagation

The fatigue crack growth experiments were conducted in combination with the real-time observation using the ZEISS Axioscope optical microscope. As a result, the entire development of slip lines from beginning to the end can be clearly observed. Referring to the images of different crack lengths in the following Fig A1, it can be seen that when the crack length is 2.45 mm, no slip line appears in the red rectangle region. However, with the increase of the crack length to 2.75 mm, a high number of slip lines can be seen on both sides of the crack, as highlighted in the red rectangle region. It is obvious that these black lines do not match all the scratches.

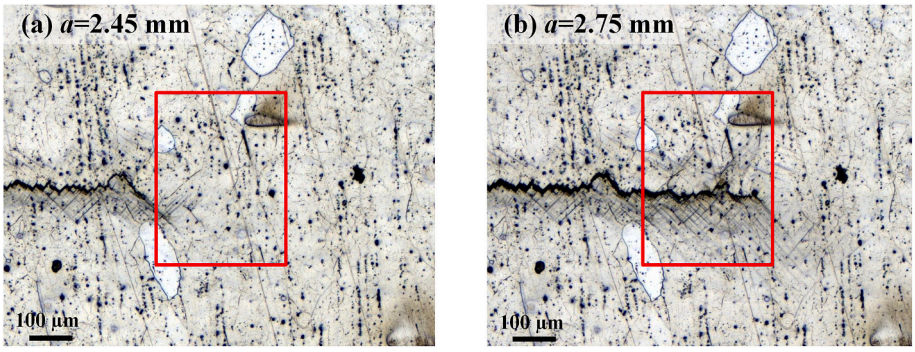

Fig. A1. Observation of slip lines during the crack propagation (a) $a = 2.45$ mm; (b) $a = 2.75$ mm.

References

[1] E. Hosseini, V. Popovich, A review of mechanical properties of additively manufactured Inconel 718, Addit. Manuf. 30 (2019) 100877.
[2] C. Panwisawas, Y. Tang, R.C. Reed, Metal 3D printing as a disruptive technology for superalloys, Nat. Commun. 11 (2020) 1–4.
[3] N. Raghavan, R. Dehoff, S. Pannala, S. Simunovic, M. Kirka, J. Turner, N. Carlson, S.S. Babu, Numerical modeling of heat-transfer and the influence of process parameters on tailoring the grain morphology of IN718 in electron beam additive manufacturing, Acta Mater. 112 (2016) 303–314.
[4] H. Helmer, A. Bauereiß, R.F. Singer, C. Körner, Grain structure evolution in Inconel 718 during selective electron beam melting, Mater. Sci. Eng. 668 (2016) 180–187.
[5] S.H. Sun, Y. Koizumi, et al., Electron beam additive manufacturing of Inconel 718 alloy rods: impact of build direction on microstructure and high-temperature tensile properties, Addit. Manuf. 23 (2018) 457–470.
[6] M. Ni, et al., Anisotropic tensile behavior of in situ precipitation strengthened Inconel 718 fabricated by additive manufacturing, Mater. Sci. Eng. 701 (2017) 344–351.
[7] X. Wang, T. Keya, K. Chou, Build height effect on the Inconel 718 parts fabricated by selective laser melting, Procedia Manuf. 5 (2016) 1006–1017.
[8] S. Goel, M. Ahlfors, F. Bahbou, S. Joshi, Effect of different post-treatments on the microstructure of EBM-built alloy 718, J. Mater. Eng. Perform. 28 (2019) 673–680.
[9] D. Deng, J. Moverare, R.L. Peng, H. Söderberg, Microstructure and anisotropic mechanical properties of EBM manufactured Inconel 718 and effects of post heat treatments, Mater. Sci. Eng. 693 (2017) 151–163.
[10] M. Ni, et al., Anisotropic tensile behavior of in situ precipitation strengthened Inconel 718 fabricated by additive manufacturing, Mater. Sci. Eng. 701 (2017) 344–351.
[11] E. Sadeghi, P. Karimi, R. Esmaeilizadeh, F. Berto, S. Shao, J. Moverare, E. Toyserkani, N. Shamsaei, A state-of-the-art review on fatigue performance of powder bed fusion-built alloy 718, Prog. Mater. Sci. 133 (2013) 101066.
[12] S.Y. Liu, S. Shao, H. Guo, R. Zong, C.X. Qin, X.Y. Fang, The microstructure and fatigue performance of Inconel 718 produced by laser-based powder bed fusion and post heat treatment, Int. J. Fatig. 156 (2022) 106700.
[13] Z.S. Hosseini, M. Dadfarnia, B.P. Somerday, P. Sofronis, R.O. Ritchie, On the theoretical modeling of fatigue crack growth, J. Mech. Phys. Solid. 121 (2018) 341–362.
[14] R. Konečná, L. Kunz, G. Nicoletto, A. Bača, Long fatigue crack growth in Inconel 718 produced by selective laser melting, Int. J. Fatig. 92 (2016) 499–506.
[15] S. Dziuba, S. Duda, K. Gruber, P. Szymczyk-zi, Fatigue crack growth characterization of Inconel 718 after additive manufacturing by laser powder bed fusion and heat treatment, Int. J. Fatig. 166 (2023) 107287.
[16] T. Brynk, et al., Fatigue crack growth rate and tensile strength of Re modified Inconel 718 produced by means of selective laser melting, Mater. Sci. Eng. 698 (2017) 289–301.
[17] X. Yu, et al., Microstructure and fatigue crack growth behavior of Inconel 718 superalloy manufactured by laser directed energy deposition, Int. J. Fatig. 143 (2021) 106005.
[18] A.R. Balachandramurthi, J. Moverare, N. Dixit, D. Deng, R. Pederson, Microstructural influence on fatigue crack propagation during high cycle fatigue testing of additively manufactured Alloy 718, Mater. Char. 149 (2019) 82–94.
[19] S. Ghorbanpour, et al., Effect of microstructure induced anisotropy on fatigue behaviour of functionally graded Inconel 718 fabricated by additive manufacturing, Mater. Char. 179 (2021) 111350.
[20] A.R. Balachandramurthi, J. Moverare, T. Hansson, R. Pederson, Anisotropic fatigue properties of alloy 718 manufactured by electron beam powder bed fusion, Int. J. Fatig. 141 (2020) 105898.
[21] D. Deng, R.L. Peng, J. Moverare, On the dwell-fatigue crack propagation behavior of a high strength superalloy manufactured by electron beam melting, Mater. Sci. Eng. 760 (2019) 448–457.
[22] M.J. Mian, J. Razmi, L. Ladani, Defect analysis and fatigue strength prediction of as-built Ti6Al4V parts, produced using electron beam melting (EBM) AM technology, Materialia 16 (2021).
[23] M.J. Mian, J. Razmi, L. Ladani, Mechanical behavior of electron beam powder bed fusion additively manufactured Ti6Al4V parts at elevated temperatures, ASME. J. Manuf. Sci. Eng. 143 (2) (2020) 021013.
[24] Y. Yao, C. Xing, H. Peng, H. Guo, B. Chen, Solidification microstructure and tensile deformation mechanisms of selective electron beam melted Ni3Al-based alloy at room and elevated temperatures, Mater. Sci. Eng. 802 (2021) 140629.
[25] H. Peng, Y. Shi, S. Gong, H. Guo, B. Chen, Microstructure, mechanical properties and cracking behaviour in a γ'-precipitation strengthened nickel-base superalloy fabricated by electron beam melting, Mater. Des. 159 (2018) 155–169.
[26] Y. Chen, B. Li, B. Chen, F. Xuan, High-cycle fatigue induced twinning in CoCrFeNi high-entropy alloy processed by laser powder bed fusion additive manufacturing, Addit. Manuf. 61 (2023).
[27] P. Nandwana, M. Kirka, A. Okello, R. Dehoff, Electron Beam Melting of Inconel 718 : Effects of Processing and Post-processing ABSTRACT, 2018 0836.
[28] Z. Dongyun, N. Wen, C. Xuanyang, L. Zhen, Effect of standard heat treatment on the microstructure and mechanical properties of selective laser melting manufactured Inconel 718 superalloy, Mater. Sci. Eng. 644 (2015) 32–40.
[29] T. Trosch, J. Strößner, R. Völkl, U. Glatzel, Microstructure and mechanical properties of selective laser melted Inconel 718 compared to forging and casting, Mater. Lett. 164 (2016) 428–431.
[30] J. Strößner, M. Terock, U. Glatzel, Mechanical and microstructural investigation of nickel-based superalloy IN718 manufactured by selective laser melting (SLM), Adv. Eng. Mater. 17 (2015) 1099–1105.
[31] J.P. Choi, et al., Densification and microstructural investigation of Inconel 718 parts fabricated by selective laser melting, Powder Technol. 310 (2017) 60–66.
[32] Y.L. Kuo, S. Horikawa, K. Kakehi, The effect of interdendritic δ phase on the mechanical properties of Alloy 718 built up by additive manufacturing, Mater. Des. 116 (2017) 411–418.
[33] A. Sengupta, et al., Tensile behavior of a new single crystal nickel-based superalloy (CMSX-4) at room and elevated temperatures, J. Mater. Eng. Perform. 3 (1994) 664–672.
[34] M.R. Gotterbarm, et al., Small scale testing of IN718 single crystals manufactured by EB-PBF, Addit. Manuf. 36 (2020) 101449.
[35] Y.J. Liu, et al., Microstructure, defects and mechanical behavior of beta-type titanium porous structures manufactured by electron beam melting and selective laser melting, Acta Mater. 113 (2016) 56–67.
[36] S.H. Sun, et al., Electron beam additive manufacturing of Inconel 718 alloy rods: impact of build direction on microstructure and high-temperature tensile properties, Addit. Manuf. 23 (2018) 457–470.
[37] M.M. Kirka, F. Medina, R. Dehoff, A. Okello, Mechanical behavior of post-processed Inconel 718 manufactured through the electron beam melting process, Mater. Sci. Eng. A 680 (2017) 338–346.
[38] C. Mercer, A. Soboyejo, W.O. Soboyejo, Micromechanisms of fatigue crack growth in a forged Inconel 718 nickel-based superalloy, Mater. Sci. Eng. 270 (1999) 308–322.
[39] N. Kouraytem, J. Varga, B. Amin-Ahmadi, et al., A recrystallization heat-treatment to reduce deformation anisotropy of additively manufactured Inconel 718, Mater. Des. 198 (2021) 109228.
[40] R.D. Doherty, et al., Current issues in recrystallization: a review, Mater. Today 1 (1998) 14–15.
[41] D.A. Hughes, N. Hansen, D.J. Bammann, Geometrically necessary boundaries, incidental dislocation boundaries and geometrically necessary dislocations, Scripta Mater. 48 (2003) 147–153.
[42] T. Zhai, A.J. Wilkinson, J. Martin, A crystallographic mechanism for fatigue crack propagation through grain boundaries, Acta Mater. 48 (2000) 4917–4927.
[43] R. Bao, X. Zhang, Fatigue crack growth behaviour and life prediction for 2324-T39 and 7050-T7451 aluminium alloys under truncated load spectra, Int. J. Fatig. 32 (7) (2010) 1180–1189.

[44] T. Zhang, et al., Investigation of fatigue crack propagation mechanisms of branching crack in 2324-T39 aluminum alloy thin plates under cyclic loading spectrum, Int. J. Fatig. 82 (3) (2016) 602–615.
[45] V.G. Ukandgaonker, P.J. Awasare, A new criterion for fracture initiation, Eng. Fract. Mech. 51 (2) (1995) 265–274.
[46] K.J. Chang, On the maximum strain criterion – a new approach to the angled crack Problem, Eng. Fract. Mech. 14 (1) (1981) 107–124.
[47] F. Erdogan, G.C. Sih, On the crack extension in plates under plane loading and transverse shear, Journal of Basic Engineering 85 (4) (1963) 519–525.
[48] K.K. Shi, L.X. Cai, S. Qi, C. Bao, A prediction model for fatigue crack growth using effective cyclic plastic zone and low cycle fatigue properties, Eng. Fract. Mech. 158 (2016) 209–219.
[49] W. Krzysztof, The fatigue crack growth rate and crack opening displacement in 18G2A-steel under tension, Int. J. Fatig. 39 (2012) 25–31.